WILEY | Hindawi

Research Article

Research on Pressure Relief Method of Close Floor Roadway in Coal Seam Based on Deformation and Failure Characteristics of Surrounding Rock in Deep Roadway

Jianjun Cao [iD],[1,2] **Benqing Yuan** [iD],[1,2,3] **Siqian Li**,[1,2] **Zunyu Xu**,[1,2] **Qihan Ren**,[1,2] **and Zhonghua Wang**[1,2,4]

[1]*CCTEG Chongqing Research Institute, Chongqing 400037, China*
[2]*State Key Laboratory of the Gas Disaster Detecting, Preventing and Emergency Controlling, Chongqing 400037, China*
[3]*Anhui University of Science and Technology, Huainan 232001, China*
[4]*Shandong University of Science and Technology, Qingdao 266590, China*

Correspondence should be addressed to Benqing Yuan; yuanbengqing3@163.com

To solve the high-stress hazard faced in the process of deep mining process, the pressure relief characteristics of gas bearing coal and the deformation characteristics of surrounding rock in deep roadway are studied by means of laboratory test, similar simulation analysis, and field investigation. The investigation results and engineering application showed that the specimens could more easily reach the failure point due to the axial pressure relief under high confining pressure. In addition, the deformation and failure degree of the surrounding rock was higher due to the disturbance from the deep high-stress roadway. The scope of the height affected by the pressure relief of the overlying strata reached above 10 m. Moreover, the initial gas emission could reach 4.41–14.39 times that of the original coal seam by drilling a hole in the coal seam at 10 m from the roof. Thus, the short-distance floor roadway exerted an obvious pressure relief effect on the overlying coal seam.

1. Introduction

As the coal mining depth is increased and the gas permeability of deep coal seams is further degraded in China [1, 2], for the single outburst coal seam or coal seam group without exploitation of the protective layer, the coal roadway strips at the outburst coal seam will be initially exploited, and the outburst prevention measure is still mainly to drill crossing holes on the floor roadway for the gas preextraction [3–5]. The difficulty in the drilling construction under deep high ground stress condition is significantly aggravated, and the gas preextraction further enhances the ground stress-dominated dynamic danger [6–9]. Various pressure relief and permeability enhancement technologies, such as hydraulic flushing [10, 11], hydrofracturing [12, 13], hydraulic slotting [14, 15], presplitting blasting [16, 17], cumulative blasting [18, 19], and CO_2 presplitting blasting

[20], have been successively proposed at home and abroad. Hydraulic reaming is carried out by conveying high-pressure water to the reaming drill pipe through an underground emulsion pump (31.5 MPa). Continuous reaming of high-pressure water jet along the radial direction of drilling hole is formed through reaming drill bit or jet device. However, the depth of reaming hole is limited due to the influence of high-pressure water resistance along the path, and the maximum depth is generally not more than 60 m. Hydraulic fracturing is performed by injecting high-pressure water into sealing boreholes through a fracturing pump set (40~70 MPa). The fracture was fractured by high-pressure water in the original coal body, but the uniformity was poor after fracturing, and there were obvious stress and gas rich areas. Currently, hydraulic fracturing pump sets are generally large in volume, high in failure rate, and poor in downhole applicability. Hydraulic slotting is separated

by radial high-pressure water jet through ultrahigh pressure clean water pump (70~100 MPa) and high-pressure sealing drill pipe in slotting bit. The high pressure hydraulic slotting has good slotting effect on medium hard coal seam, but it cannot form flat disc slotting groove for soft coal seam, and the working pressure is high, so there is a certain safety hazard. The exposed area of coal seam in coal hole section is increased by mechanical cutting through secondary mechanical reaming. However, the increase of the overall reaming radius is limited. At present, the maximum aperture of reaming using equipment machinery is only 300 mm, which is easy to induce dynamic phenomenon for coal seam reaming with higher gas content and pressure, i.e., greater outburst risk, and brings certain security risks. Controlled presplitting blasting is to produce a large number of cracks around the blast hole through the blasting effect of explosives in the coal and rock stratum, increase the permeability of coal, and improve the extraction effect. However, for the deep soft coal seam, the hole forming effect is poor, the charging is difficult, and the blasting pressure relief and permeability enhancement effect is not ideal, which is easy to produce misfire and bring potential safety hazards.

Given the complex and diversified stress field evolution of surrounding rock in deep roadway, the large deformation and strong rheological properties of surrounding rock, the brittleness–ductility transformation of coal and rock mass, and the mutability of dynamic response [21, 22], a pressure relief and permeability enhancement method of short-distance floor roadway in deep coal seam was investigated and formed. The comprehensive study shows that in view of the high stress hazard of deep mine, the stress level of overlying coal rock mass can be reduced in advance by laying near floor roadway at a certain distance below the coal roadway to be excavated. The pressure relief method of near floor roadway proposed in this paper is feasible and can provide reference for the prevention and control of mine disasters under similar conditions.

2. Mechanical Characteristic Test of Pressure Relief in Gas-Bearing Coal

2.1. Testing System and Program

2.1.1. Testing System. The gas–solid coupling seepage system [23] used in the test was mainly composed of four major parts, namely, pressure loading chamber, hydraulic servo control system, gas seepage system, and data acquisition system. The test device is shown in Figure 1, which can test the coupling relationship between mechanical properties and seepage characteristics of coal under different stress paths.

The pressure chamber provides the required stress environment for the test. The frame system is composed of 4 columns and upper and lower supports. The true three-axis pressure chamber is embedded in the circular groove set by the lower support, the cylinder height is 494 mm, the inner diameter is 500 mm, and the "O" type sealing ring is installed at the joint. Three-way stress loading and unloading is controlled by hydraulic servo system and automatically controlled by constant speed and constant pressure

FIGURE 1: Physical diagram of gas–solid coupling coal seepage test system.

metering pump. It has two working modes of constant current and constant pressure. At the same time, it is equipped with touch-type keyboard and data display screen, which can easily set and intuitively display the operating status, pressure, and flow. It is through the standard data interface to ensure that the computer to pressure, flow, pump, or pump volume and other parameters can be real-time acquisition. The gas seepage system consists of high-pressure gas cylinders, gas guide pipes, pressure reducing valves, and flowmeters. The gas enters the pressure chamber through the pressure reducing valve, flows through the coal specimen, and then passes through the mass flowmeter. The pressure copper pipe of 6 mm is the gas guide pipe, which is connected with a conical head to ensure good air tightness of the seepage system. Three-way automatic control of stress loading and unloading parameters and stress path and continuous and automatic data acquisition ensure the reliability of data.

2.1.2. Testing Program. In this paper, the variation characteristics of stress, deformation, and permeability of coal under axial stress unloading path were studied. The gas-bearing coal was loaded to 80% of the compressive strength of the test coal mass. After the deformation and seepage of the coal mass became stable, the axial pressure or confining pressure was kept constant, and the axial pressure was unloaded at a rate of 0.01 N/s until the failure of coal specimen. The stress loading and unloading path is shown in Figure 2.

Given that the coal mass structure was soft, the raw coal specimen was difficult to fabricate with a low success rate; conversely, the differences among the coal specimens in their physical and mechanical parameters, such as compressive strength and tensile strength, were minor due to the standard fabrication process; the influence of specimen difference on the experimental results was basically eliminated, and the physical and mechanical properties of coal could be well reflected [24]. Hence, standard rectangular-shaped coal specimens were used in this test. Specifically, the fresh coal samples are ground and ground on the pulverizing machine, screened out the same amount of 20~40 mesh and 40~80 mesh coal sample preparation base material, mixed evenly with water, then put into the specimen forming device, and pressed on the 100 T press for 30 min into rectangular
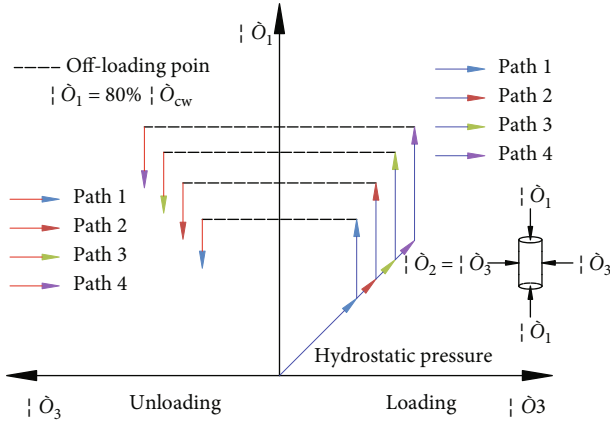
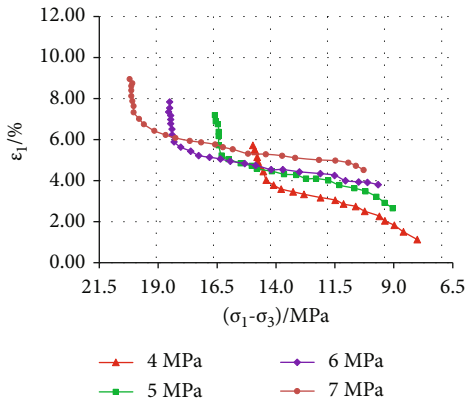FIGURE 2: Schematic of stress loading/unloading path.

FIGURE 3: Mechanical characteristic curves in the axial pressure unloading of coal specimens under a constant atmospheric pressure of 1.5 MPa and different confining pressures.

standard briquette specimen with size of 100 mm × 100 mm × 200 mm. Place in a drying oven at 80°C for 24 hours and wrap it with insurance film for later use.

2.2. Axial Unloading Characteristics under Different Confining Pressures

2.2.1. Engineering Background. This paper takes Qujiang Coal Mine as the engineering background. The mine is located in Qujiang Town, Fengcheng City, Jiangxi Province. It is 9 km long from east to west and 4.8 km wide from north to south, covering an area of 39.5988 km², and the ground elevation is +20.1~+90.8 m. Qujiang Coal Mine is the main mine of Fengcheng Mining Area, with a designed production capacity of 900,000 t/a. The current production level is -850 m level, and the buried depth of coal seam exceeds 900 m, which belongs to deep mining.

The single B_4 coal seam mined in Qujiang Coal Mine is a gently inclined medium-thick coal seam with a dip angle of 12°~14° and an average coal thickness of 2.86 m. The roof of the coal seam is intermingled with fine sandstone and mudstone with a high proportion of sandstone and good sealing performance. The bottom plate is dominated by fine, medium fine, coarse, and medium sandstone. B_4 coal seam

has high buried depth geostress, gas pressure and gas content (measured gas pressure $P_{max} = 9.2$ MPa and gas content $W = 13.5 \sim 25.3$ m³/t), soft structure (firmness coefficient $f = 0.29 \sim 0.8$), and extremely low permeability ($K = 1.7 \times 10^{-5} \sim 4.4 \times 10^{-5}$ m²/MPa²·d), it is difficult to extract gas, and it takes a long time for intensive drilling to reach the standard, and the extraction efficiency is low.

In view of the coal roadway belt, the regional predrainage gas outburst prevention measures are mainly implemented through the construction of dense drilling holes through the floor (the spacing between them is 3.0 m × 3.0 m). The gas drainage from drilling holes reduces the energy of gas outburst, but it is difficult to eliminate the harm of high in situ stress in deep mining. In the process of drilling construction, abnormal phenomena such as jet holes and drill clamping often occur.

2.2.2. Mechanical Characteristics. The axial pressure unloading test under the conventional triaxial stress condition with constant pressure and different confining pressure is conducted. The axial pressure and confining pressure are, respectively, loaded to different hydrostatic pressure levels (successively $\sigma_1 = \sigma_2 = \sigma_3 = 4$ MPa, 5 MPa, 6 MPa, and 7 MPa), and gas with pressure $P = 1.5$ MPa is introduced to keep the confining pressure unchanged. Continue to apply axial pressure to 80% of the compressive strength of coal samples under the same conditions in force control mode of 0.01 N/s, and then unload axial pressure in control mode of 0.01 N/s until coal failure occurs. The axial compressive stress–axial strain unloading curves of gas-bearing coal under constant gas pressure ($p = 1.5$ MPa) and different confining pressures ($\sigma_2 = \sigma_3 = 4, 5, 6$, and 7 MPa) are shown in Figure 3.

Under different confining pressures, the axial strain decreases rapidly at first and then slowly during the unloading process of axial stress. However, with the increase of confining pressure, the axial strain at final failure shows an increasing trend (as shown in Figure 4). When the confining pressure was elevated from 4 MPa to 7 MPa, the strain ε_{final} was increased from 1.13% to 4.52% in case of coal failure, with the increase amplitude reaching 300%. That is, the higher the confining pressure is, the more easily the specimen under axial pressure relief will reach the failure point.

3. Simulation Analysis of Deformation Characteristics of Surrounding Rock in Deep Roadway

3.1. Similar Simulation Scheme and Parameter Determination

3.1.1. Testing System. A two-way four-plane load-adjustable multifunctional similar simulation testing device [25] was used to simulate deep underground engineering. This device mainly included a model steel truss, a constraining channel steel, a transparent organic glass viewing window (800 mm × 900 mm), and a loading system. The effective dimensions were 3,000 mm × 2,000 mm × 200 mm. A picture of this device is shown in Figure 5.

(a) Failure strength
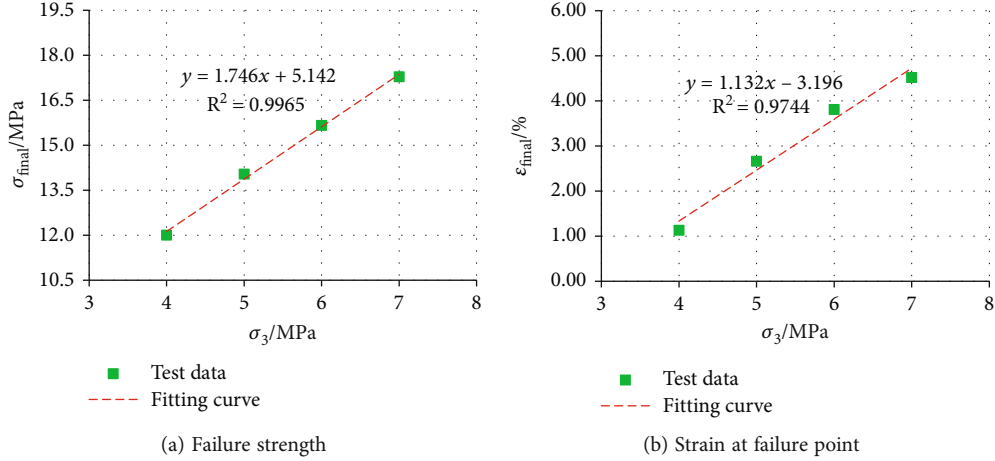

(b) Strain at failure point

FIGURE 4: Strength and strain change curves at the failure point in the axial pressure unloading of coal specimens under a constant atmospheric pressure of 1.5 MPa and different confining pressures.
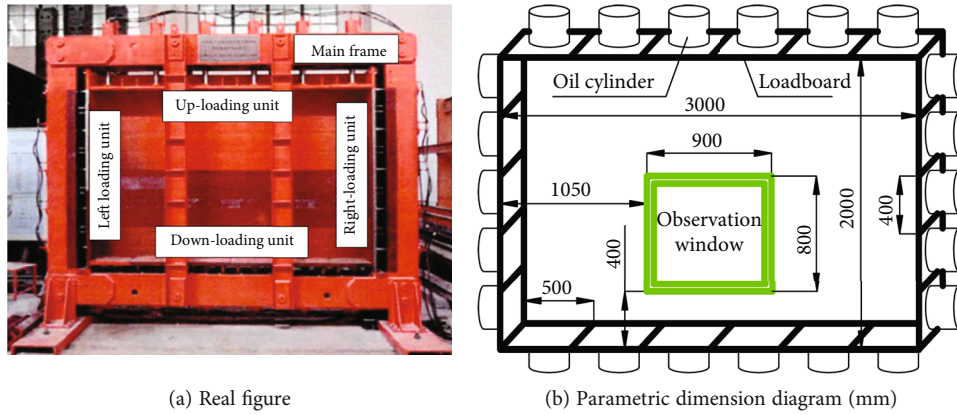

(a) Real figure

(b) Parametric dimension diagram (mm)

FIGURE 5: Picture of the testing device for similar simulation.

3.1.2. Experimental Parameters. According to the literature [26], the geometric similarity ratio is generally 20–300 in the similar simulation of mining and 20–50 in the simulation of underground chamber and tunnel (roadway). By combining the size of the viewing window in the actual testing device for the similar simulation, the geometric similarity ratio was taken as $\alpha_l = 25 : 1$ in this study, and the roadway width and height were calculated as 160 mm and 120 mm, respectively.

The average density of field surrounding rock in the roadway was 2.5 g/cm^3, and that of similar material matched in the laboratory was 1.56 g/cm^3. Thus, the similarity ratio of the volume weight was $\alpha_r = 1.6$, that of stress was $\alpha_\sigma = \alpha_l \times \alpha_r = 40$, and that of Poisson's ratio was constantly 1. On the basis of the similar three theorems, the similarity ratio of time was obtained as $\alpha_t = (\alpha_l)^{0.5} = 5$, and it was taken as 6 to facilitate the time simulation. That is, 4 h simulation was equivalent to 24 h field operation.

According to the principle of similarity, 14 anchor bolts and 3 anchor cables shall be arranged in each row, with a total of 84 anchor bolts and 18 anchor cables. In consideration of ineradicable friction effect, supporting intensity, and density of front and rear baffles in the model, the support parameters were adjusted, 4 rows were arranged in the front and back, and 10 anchor bolts and 3 anchor cables were arranged in each row, with a total of 40 anchor bolts and 12 anchor cables.

The simulated aggregate is river sand with particle size of 0.2~0.5 mm brushed by 250 mesh sieve, the cementitious material is freshly burned lime and hydrated gypsum, and 40-mesh mica powders were applied on the bedding plane. On the basis of the corresponding matching number, the matching ratio of similar simulation materials was determined, as shown in Table 1.

3.1.3. Monitoring Method. A totally enclosed-type test rack was used in the simulation. The strain inside the surrounding rock was monitored with a distributed optical fiber. The distributed optical fiber monitoring equipment and measuring line layout are presented in Figure 6.

The surface displacement was observed by high-definition digital camera. To clearly observe the fracture and displacement development on the model surface, the observed surface at the viewing window part was uniformly whitewashed, the vertical crossing measuring lines were marked using ink lines, and the displacement measuring point layout in the viewing window is shown in Figure 7.

TABLE 1: Matching materials in similar simulation test and their use levels.

| Serial number	Rock stratum name	Seam height/ mm	Proportion number	Amount/kg			Total/ kg	Water quantity/kg	Remark
				River sand	Lime	Gypsum			
1	Gritstone	100	4 : 0.6 : 0.4	115.2	17.2	11.6	144.0	14.4	
2	Sandy shale	100	6 : 0.7 : 0.3	123.6	14.4	6.0	144.0	14.4	Pavement stratum
3	Fine sandstone	100	5 : 0.6 : 0.4	120.0	14.4	9.6	144.0	14.4	
4	Medium-fine grained sandstone	120	5 : 0.6 : 0.4	144.0	17.9	11.4	172.8	17.4	Layer of floor roadway
5	Sandy shale	300	6 : 0.7 : 0.3	370.2	43.2	18.6	432.0	43.2	
6	Mudstone	100	7 : 0.7 : 0.3	126.0	12.6	5.4	144.0	14.4	
7	Coal seam	120	10 : 0.5 : 0.5	157.0	7.9	7.9	172.8	17.3	
8	Mudstone	100	7 : 0.7 : 0.3	126.0	12.6	5.4	144.0	14.4	Roof layer
9	Fine sandstone	200	5 : 0.6 : 0.4	240.0	28.8	19.2	288.0	28.8	
10	Mudstone	130	7 : 0.7 : 0.3	163.8	16.4	7.0	187.2	18.7	
11	Fine sandstone	230	5 : 0.6 : 0.4	288.0	34.5	23.1	345.6	34.6	
12	Fine sandstone	200	5 : 0.6 : 0.4	252.0	30.2	20.2	302.4	30.2	
Accumulate		1,800	/	2,225.8	250.1	145.4	2,620.8	262.2	
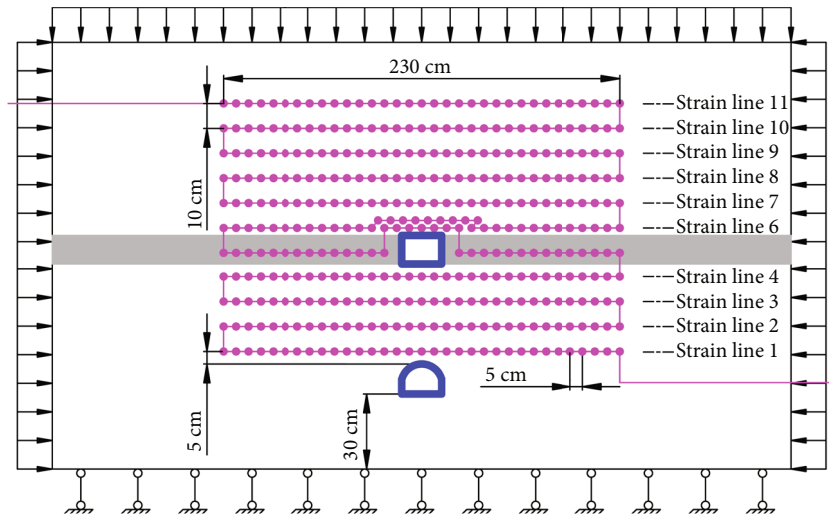
FIGURE 6: Strain measuring line and monitoring point layout plan of distributed optical fiber.
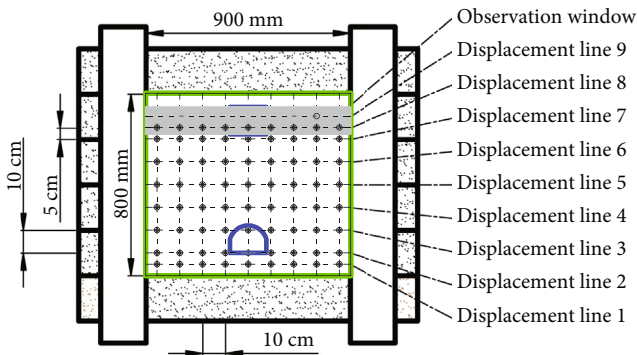

FIGURE 7: Displacement measuring line and monitoring point layout plan of viewing window.

During the pressurization process, the strain was acquired via a distributed optical fiber, the surface displacement was observed using a high-precision digital camera, and the failure was photographed synchronously. In the steady pressure phase, the strain data acquisition frequency was 4 h each time, and it was 1 h each time in other phases. The photographing frequency was 2 h each time in case of no obvious changes and 0.5 h each time in case of evident changes.

3.2. Deformation and Failure Characteristic Analysis of Overlying Strata after Floor Roadway Excavation
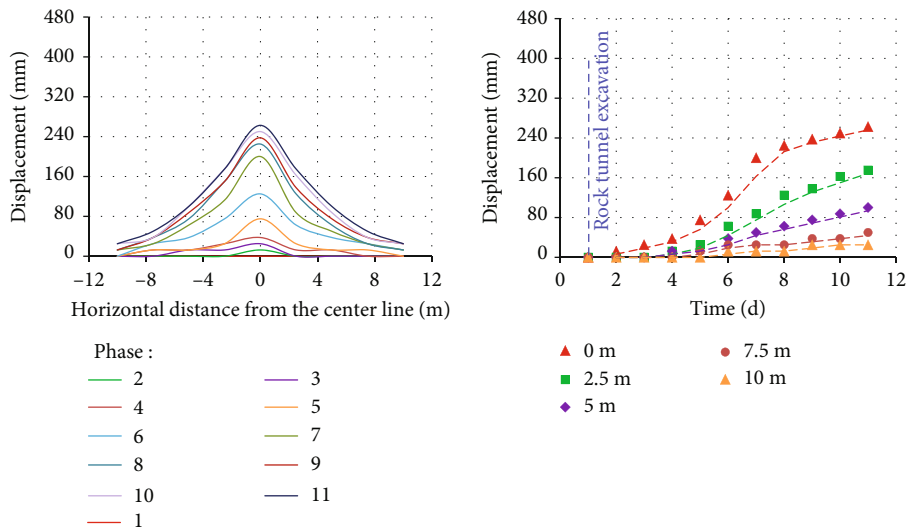
3.2.1. Displacement Evolution Characteristics of Overlying Strata.
The vertical displacement changes on the model surface in different loading phases were collected through the near-view photographing technology of a high-definition digital camera, and the changes at some measuring lines
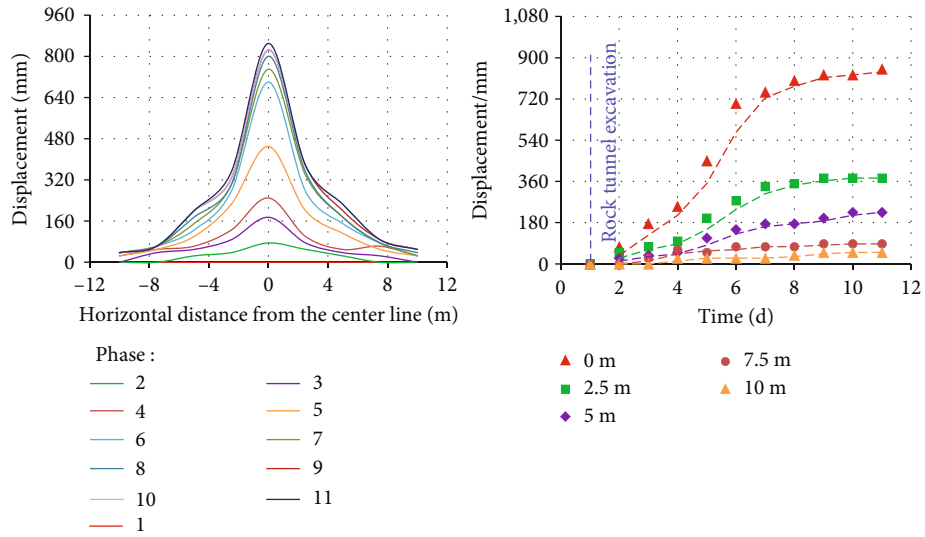
(a) Displacement line 4 at 2 m from the roadway roof
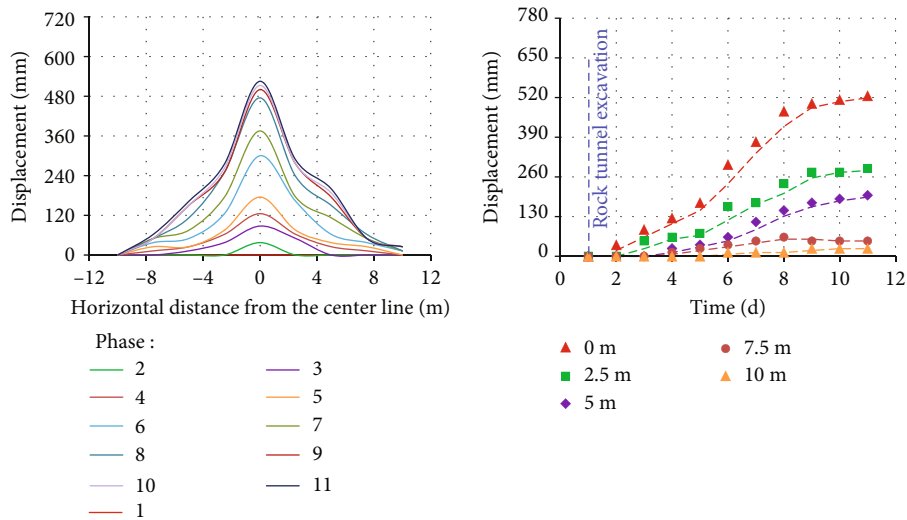
(b) Displacement line 6 at 7 m from the roadway roof

(c) Displacement line 9 at 12 m from the roadway roof (stratum of coal seam)

Figure 8: Roof displacement curves in different loading phases after floor roadway excavation.

(a) Phase 1

(b) Phase 3

(c) Phase 5
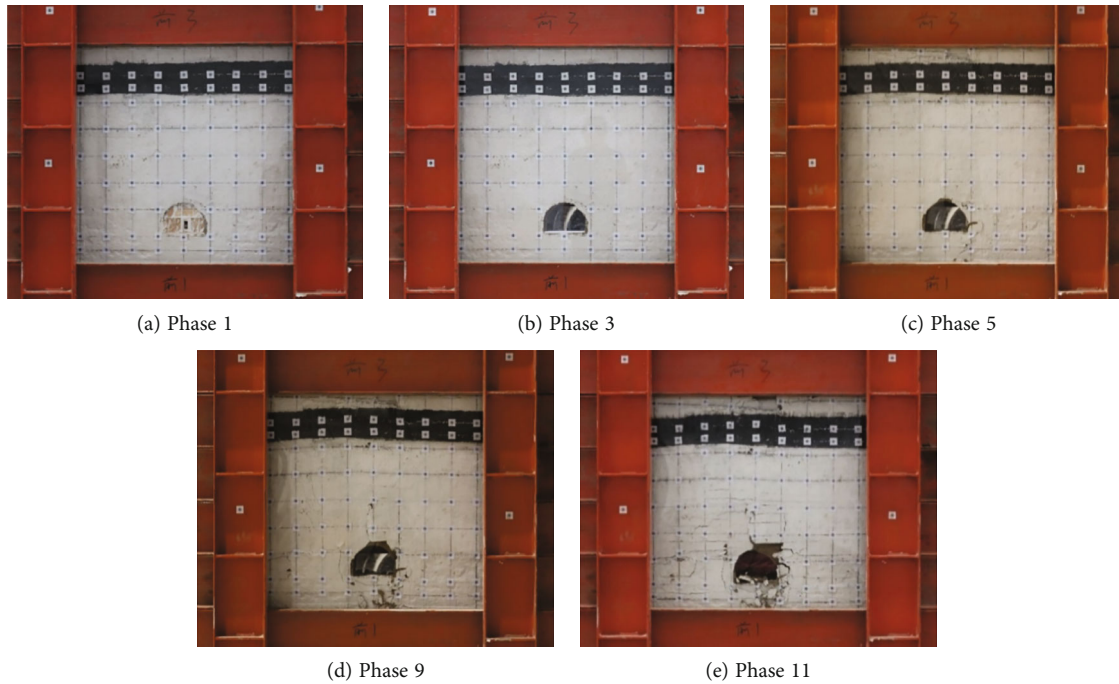
(d) Phase 9

(e) Phase 11

Figure 9: Fracture development characteristics on the roadway surface in different loading phases.

are displayed in Figure 8 (the following related data were all the original sizes after conversion; the displacement field formed in loading phase 1 was taken as base point 0; the left side of the roadway center line was negative, whereas the right side was positive).

As shown in Figure 8, in the steady pressure phase (phase 1) and initial loading phase (phases 2–4), the subsidence of the roadway surface was minor, and the deformation basically presented the " ⠿⠿ ?"-shaped symmetric distribution characteristic; as the load was increased (phases 2–5), the subsidence of the roadway surface was enlarged, and the deformation basically showed "V"-shaped symmetric distribution characteristics. That is, the subsidence displacement at the roof position, where the left and right sides of the same measuring line were equally distant from the roadway center line, was basically identical, presenting the axisymmetric laws. The more distant from the roadway center line was, the smaller the displacement would be. The maximum displacement appeared at the middle of the roadway, specifically as follows. After the roadway excavation, from loading phase 2 to phase 11 (1–11 d after the excavation), the surface subsidence displacement in the roadway center at 2 m from the roof was elevated from 75 mm to 850 mm, that in the roadway center at 7 m from the roof was increased from 37.5 mm to 525 mm, and that in the roadway center at 12 m from the roof (stratum of coal seam) was increased from 12.5 mm to 262.5 mm.

The observation line 9 of the horizon where the coal seam is located (within the range of 10~13 m above the floor roadway) is in the loading phase 11, and the corresponding subsidence at the distance of 2.5 m, 5 m, 7.5 m, and 10 m from the roadway center is 170 mm, 98 mm, 48 mm, and 24 mm, respectively. The comprehensive analysis indicated

that the scope of influence of the floor roadway excavation under the effect of mine ground pressure reached above 10 m when the burial depth of Qujiang Coal Mine was 800 m.

3.2.2. Fracture Development Characteristics in Overlying Strata. With the increase in the load applied to the upper, lower, left, and right loading units, the appearance and development process of fractures around the roadway could be intuitively displayed through the high-definition camera. After the experimental preparations were made, the whole overlying strata movement and fracture development and evolution process during the loading process after the roadway excavation was completely recorded, as shown in Figure 9. The fractures at the roadway roof were continuously developing and propagating with the increase in the load applied. Relative to the three-phase evolution characteristics of the displacement of the surrounding rock, the fracture development at the roadway roof was also basically divided into three phases: initial phase nearly without fracture, slow development phase, and intense development phase.

In loading phases 1–4, the maximum pressure reached 5 MPa at the upper and lower loading units and that at the left and right loading units reached 4 MPa. In this period, the pressure load borne by the model was relatively small. Specifically, the fractures between the internal rock strata were continuously compacted, the overall rock strata at the roof subsided, and almost no fractures appeared.

In loading phase 5, the fractures that deviated from the arch corner to the floor at the roadway center were initially generated at the right arch corner of the roadway due to shear dislocation, with the extended length of about
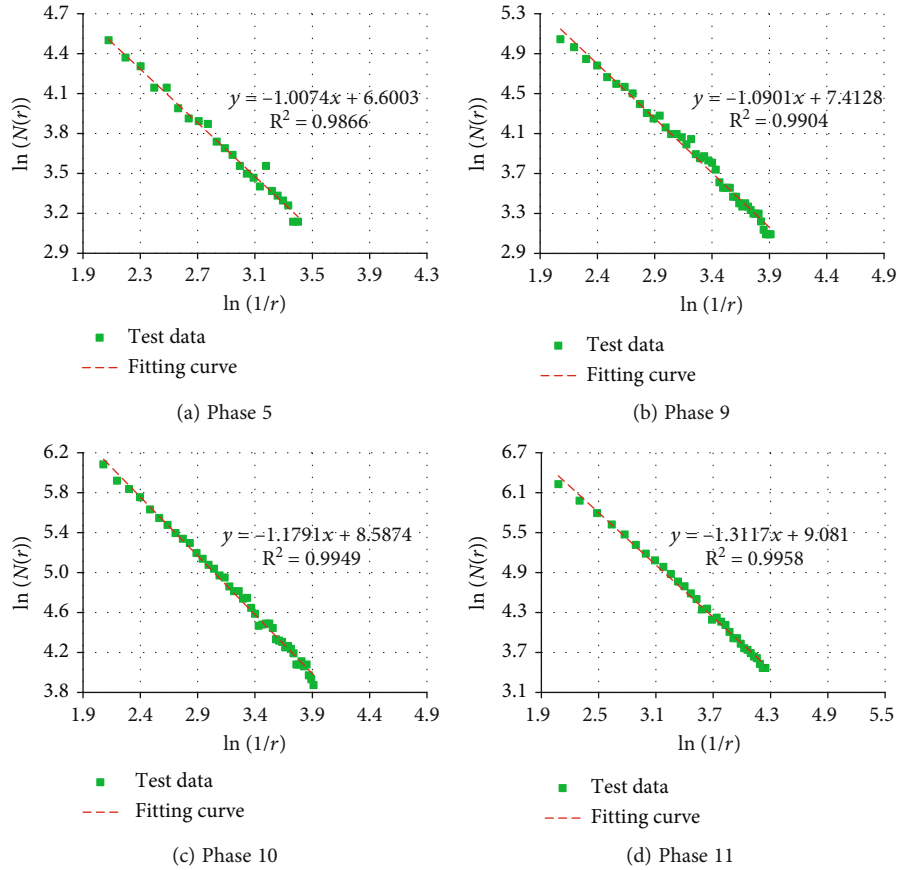
(a) Phase 5

(b) Phase 9

(c) Phase 10

(d) Phase 11

FIGURE 10: Curve chart of fractal dimension calculation for fractures in different loading phases.

2.5 mm. Almost at the same time, an inverse "L"-shaped fracture developed at the roadway roof from the roadway center, with the vertical length of about 2.4 m and transverse length of about 2.6 m. As the load was increased until phase 9, the original fractures within 3 m range at the roadway roof continuously developed, propagated, and extended. Moreover, multiple transverse and vertical fractures developed at the right side of the roadway center line due to the upper load without obvious detachment. Given the stress concentration, multiple vertical fractures and a small quantity of transverse fractures appeared within 5 range at the left wall of the roadway. Long fractures were generated within 1.5 m range from the roadway floor to the undersurface under the continuous squeezing effect of the surrounding rock, with the length reaching 4 m, and small-scale floor heaving started appearing.

In the 10~11 loading phases, the surrounding rock of the roadway began to be damaged, the existing cracks developed violently, some cracks formed through cracks, and the block fell off on the surface of the model. In the intense fracture development phase, as the compressive strength of the material was considerably greater than the tensile strength, the original fractures at the model strata, especially the roof strata, were continuously developing under the combined action of horizontal and vertical stresses. Moreover, a large number of vertical fractures were generated due to the Pois-

son's effect, along with the rupturing phenomenon. The roof continuously subsided, the subsidence at the right side of the roof center could be evidently manifested from a macroscopic perspective, and a bulging phenomenon was prominent. Some rock strata experienced obvious shear dislocation, and the central subsidence was apparently larger than that of the rock mass at the two sides.

According to the literature, the fractal characteristics of fracture development were analyzed using box dimension in this study, and the calculation method is expressed as follows:

$$D = \lim_{r \longrightarrow 0} \left[\frac{\ln N(r)}{\ln (1/r)} \right], \qquad (1)$$

where D is the fractal dimension value based on box dimension; r denotes the radius of nonempty subset, and $r > 0$; $N(r)$ represents the least number in the covered subset A_r; A_r is an arbitrary bounded subset in the domain.

The fracture development laws in the overlying rock strata of the roadway in different loading phases were quantitatively analyzed. The fracture pictures in different loading phases were selected, followed by the grey processing, to obtain the black and white bar graph used to calculate the fractal dimension. The fracture distribution graphs in different loading phases were transformed into sketch maps. Next,

(a) Strain line 1

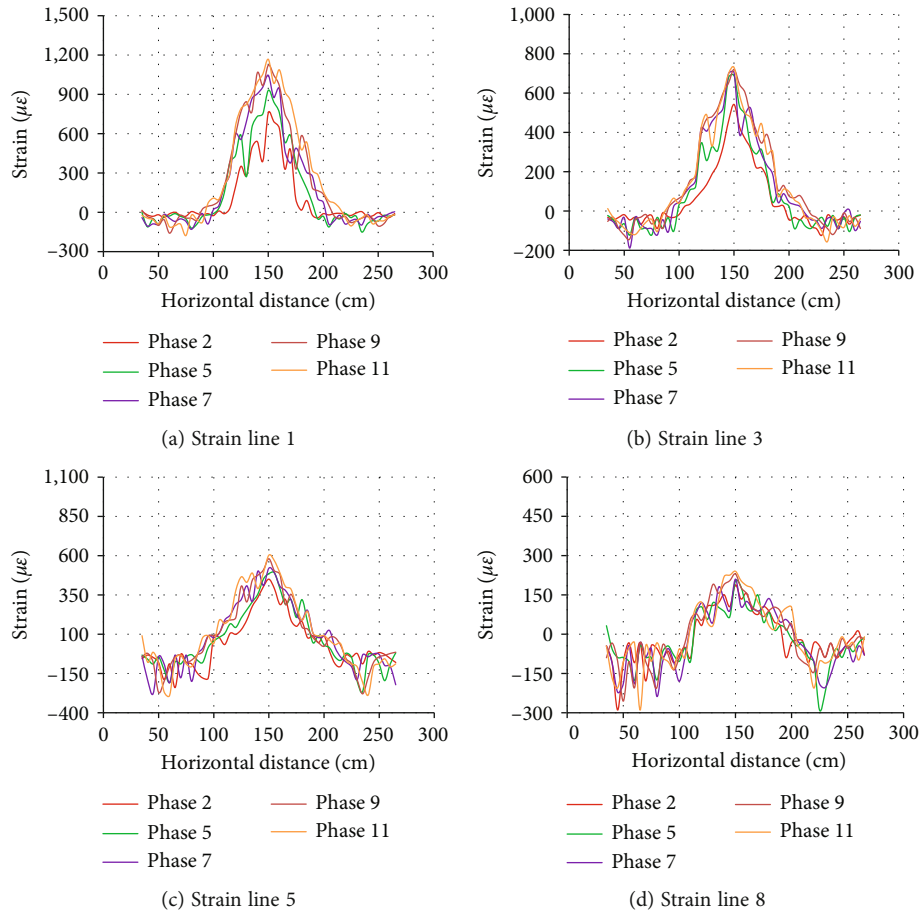(b) Strain line 3

(c) Strain line 5

(d) Strain line 8

FIGURE 11: Strain curve chart of overlying strata in different loading phases after the floor roadway excavation.

the related parameters in Equation (1) were calculated via the Fractal Fox software, and the fractal dimension shown in Figure 10 was generated. In the figure, the fractal dimension in the fracture network in the mined rock mass was presented through a straight slope.

The occupation of fractures in two-dimensional space under different loading phases reflects the dynamic evolution law of fracture network distribution, and better reveals the variation characteristics of fractures with loading phase (buried depth). In the fractal dimension calculation for fractures in different loading phases after the floor roadway excavation, the fitting precision (R^2 value) was high (over 0.99), indicating that the fractal characteristics of the fracture network evolution in the floor roadway in different loading phases were regular. After the floor roadway excavation, the fractal dimension of fractures presented an overall increasing trend with the loading phase (namely, with the increase in the pressure), being basically divided into three phases: the phase almost without fractal dimension, phase with slow dimension increase, and phase with rapid dimension reduction, which basically corresponded to the fracture development characteristics in the previous section.

3.2.3. Strain Distribution Characteristics in Overlying Strata. The data acquisition interval at the distributed optical fiber strain points used in this study was 5 cm, the length of each measuring line was 230 cm, and the collected data size was 46. Given the overall large data size, the observed data of strain measuring lines 1, 3, 5 (stratum of coal seam), and 8 at 5, 25, 45, and 75 cm from the roadway roof were calculated to form the test results of strain measuring lines in different loading phases, as shown in Figure 11. The tensile strain was set positive, whereas the compressive strain was negative.

Figure 11 shows the strains at the coal and rock strata within a certain range at the left and right sides of the roadway center line. With the roadway center line taken as the center, the strains were basically symmetrically distributed, which was nearly identical with the characteristic curve of the displacement evolution in the surrounding rock, as aforementioned. The existence of tensile strain reflected that the coal and rock strata within this range were affected by the mining disturbance, with a certain subsidence displacement. In the zone with tensile strain, the coal and rock strata were under pressure relief state, and the greater the tensile strain was, the higher the pressure relief degree would be. Compressive strain existed in the other zones, indicating that they were almost not affected by the roadway excavation. Moreover, they were basically located at the terminal line of the fracture development.
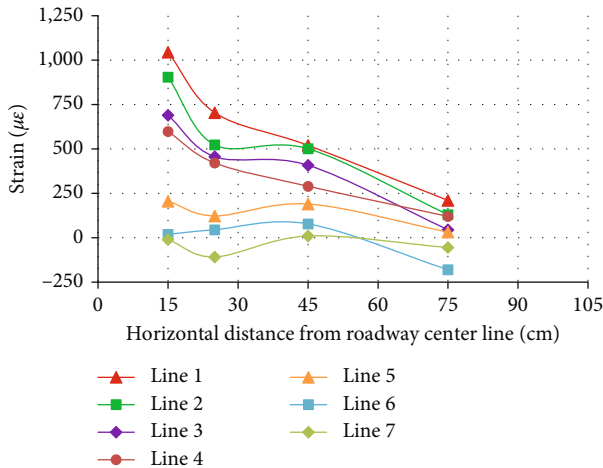
FIGURE 12: Curve chart of strain test results at different positions and measuring lines at the left side of the roadway center line (phase 7).

FIGURE 13: Drill hole layout plan.

Following the roadway excavation, the maximum tensile strain appeared nearby the roadway center. For example, the maximum tensile strains at strain measuring lines 1, 3, 5, and 8 were 1,167, 730, 603, and 240 $\mu\varepsilon$, respectively, indicating that these positions were greatly disturbed after the roadway excavation. With the increase in the distance from the roadway roof, the strain of overlying strata followed such laws. ① In the same loading phase, the tensile strain was gradually reduced. That is, the pressure relief was gradually weakened, and the strain test results at different positions and measuring lines in phase 7 are specifically shown in Figure 12. ② The ranges of tensile strain zones generated at measuring lines 1–5 were gradually enlarged. In phase 7, the ranges of tensile strain zones at measuring lines 1, 3, and 5 were 26.25, 30.00, and 31.25 m, respectively. However, the range of tensile strain zone at the coal seam roof was gradually shrunk, and that at measuring line 8 was only 23.75 m.

As the loading proceeded (i.e., the pressure applied was increased), the strain of the overlying strata basically presented the following laws. ① At the same measuring line, the range of tensile strain was gradually enlarged in phases 2–9, and that in phases 10 and 11 was almost unchanged. For example, the ranges of tensile strains at measuring line 3 in phases 2, 5, 7, 9, and 11 were 23.75, 26.25, 30.00, 31.25, and 31.25 m, respectively. ② The tensile strain value at the same measuring line was gradually enlarged. For instance, the tensile strains at measuring line 3 in phases 2, 5, 7, 9, and 11 were 542.0, 600.0, 704.0, 720.0, and 730.0 $\mu\varepsilon$, respectively.

The measuring line 5 of the coal seam is located at 11.25 m of the roadway roof. At the end of the 11th phase of loading, the tensile strain range is 31.25 m, that is, the tensile strain is generated within 15.6 m on both sides with the roadway centerline as the midpoint. Therefore, the coal seam within this range is in a pressure relief state after roadway excavation.
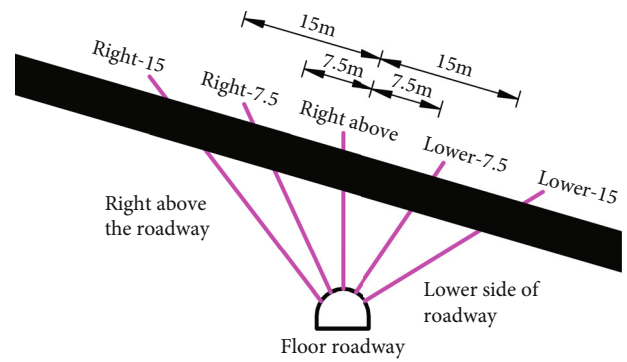
4. Engineering Application of Pressure Relief Method through Short-Distance Floor Roadway at Deep Coal Seam

4.1. Project Profile and Investigation Scheme for Application Effect. To further verify the previous study results, the outburst prevention method through the pressure–relief gas drainage in the floor roadway was applied in Fengcheng Mining Area, and the study object was 213 floor roadway in Qujiang Coal Mine. The single B_4 coal seam exploited in this mine was medium-thickness coal seam with a gentle dip. The dip angle of the coal seam was 12°–14°; the average coal thickness was 2.86 m; the coal seam roof was composed of fine sandstone and mudstone, where sandstone accounted for a high proportion with good sealing capacity; the floor was mainly composed of fine, medium, and coarse sandstone and medium sandstone. The B_4 coal seam was characterized by a large burial depth, high ground stress, gas pressure and gas content (measured gas pressure: $p_{max} = 9.2$ MPa and gas content: $W = 13.5 – 25.3$ m^3/t), loose and soft structure (firmness coefficient: $f = 0.29 – 0.8$), extremely low gas permeability ($k = 1.7 \times 10^{-5} – 4.4 \times 10^{-5}$ m^2/MPa^2·d), difficult gas extraction, long time consumed by the dense borehole drainage to reach the standard, and low extraction efficiency. Given that the geological structures were complicated in the Fengcheng Mining Area to reduce the safety risk induced by the mistaken coal uncovering, the 213 floor roadway was arranged at 10 m away from the coal seam floor in Qujiang Coal Mine, and the pressure–relief baseplates were overlapped up and down.

The pressure relief effect of the floor roadway was investigated mainly from two aspects: displacement and failure of the surrounding rock. The drill holes were arranged, as shown in Figure 13, and the investigation sites were designed, as shown in Table 2. The displacement and failure characteristics at different depths of the surrounding rock were investigated using DW-6 multipoint displacement meter and YTJ20 rock strata detection recorder, the diameter of all drill holes was $\Phi32$ mm, and the real pictures of the instruments are displayed in Figure 14.

4.2. Investigation on Pressure Relief Effect in Overlying Strata of the Roadway

TABLE 2: Investigation sites of pressure relief effect.

Mine	Floor roadway number	Distance from investigation site to head-on/m			Diameter of drill hole/mm	Investigation content
		Group 1	Group 2	Group 3		
Qujiang	213	244	208	116	32	Displacement and failure of the surrounding rock and gas flow in the drill hole

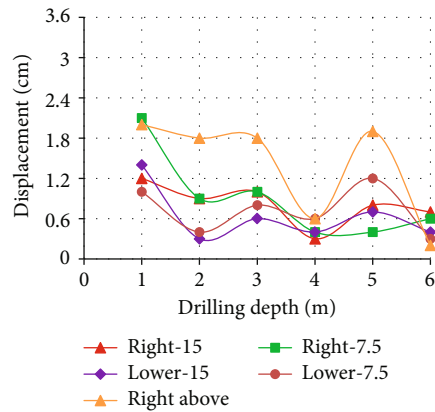(a) DW-6 multipoint displacement meter
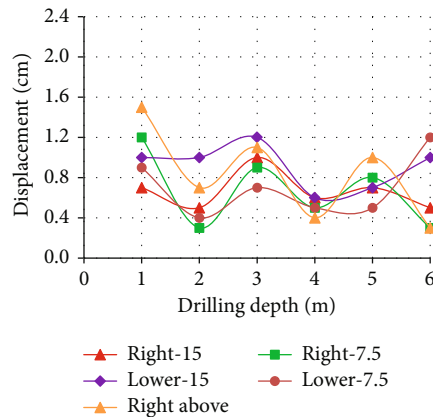
(b) YTJ20 rock strata detection recorder

FIGURE 14: Real pictures of instruments used for investigating pressure relief effect.
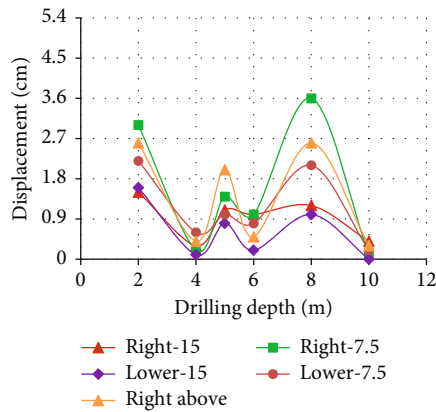
(a) Group 1 (244 m away from the tunneling head-on)

(b) Group 2 (208 m away from the tunneling head-on)

(c) Group 2 (116 m away from the tunneling head-on)

FIGURE 15: Displacement curve chart of surrounding rock in 213 floor roadway in Qujiang Coal Mine.
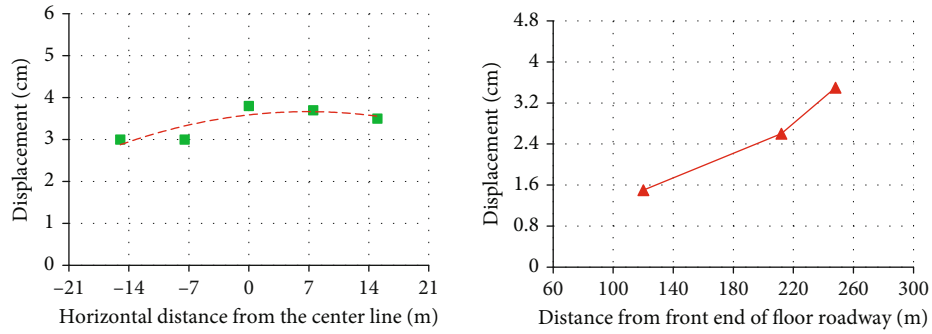
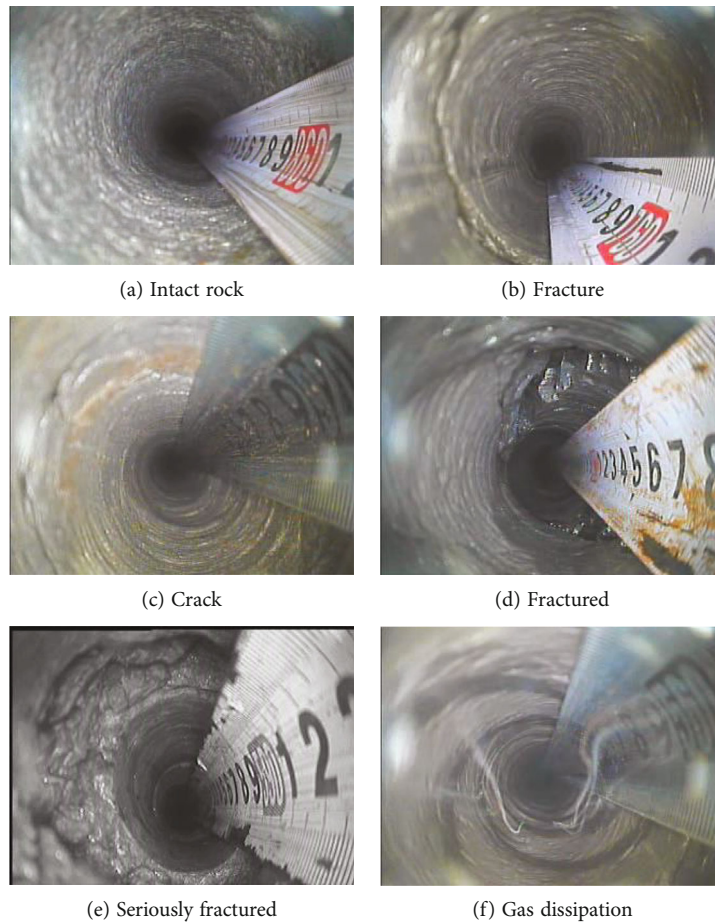FIGURE 16: Curve chart of maximum displacement of surrounding rock in 213 floor roadway of Qujiang Coal Mine.

(a) Intact rock

(b) Fracture

(c) Crack

(d) Fractured

(e) Seriously fractured

(f) Gas dissipation

FIGURE 17: Peering video screenshots of drill holes.

4.2.1. Displacement Change of Overlying Strata. A total of six measuring points were arranged in each drill hole to investigate the displacement of the surrounding rock, and the investigation results are presented in Figure 15. The displacements at different depths of drill holes were characterized by the alternate change of crest and trough, which indicated the zonal disintegration inside the surrounding rock. The crest and trough represented the failure and non-failure zones of the surrounding rock, respectively [27].

The maximum displacements on different investigated sections (sites) of the surrounding rock in the roadway were calculated, as shown in Figure 16, basically presenting the distribution characteristic of successive reduction from the roadway center line to the two sides. With the increase in the distance from the working face, the deformation of the surrounding rock in the roadway above the floor roadway became greater. In addition, the pressure relief of the surrounding rock was more sufficient, which accorded with the pressure relief law in the deep roadway and the theory of rheological effect.

4.2.2. Zonal Fracture of Surrounding Rock. The situation in the holes could be detected using a peering instrument, a steel measuring tape, and video transmission technology
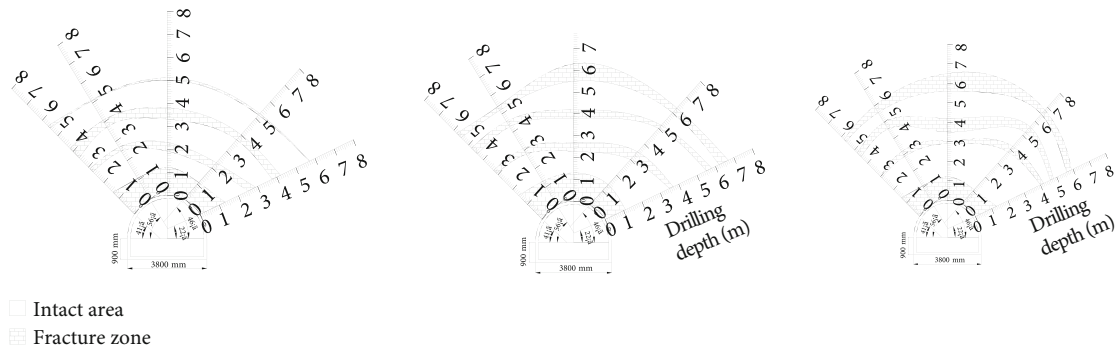
FIGURE 18: Zonal fracture of surrounding rock in 213 floor roadway of Qujiang Coal Mine.

(a) Average initial fracture position
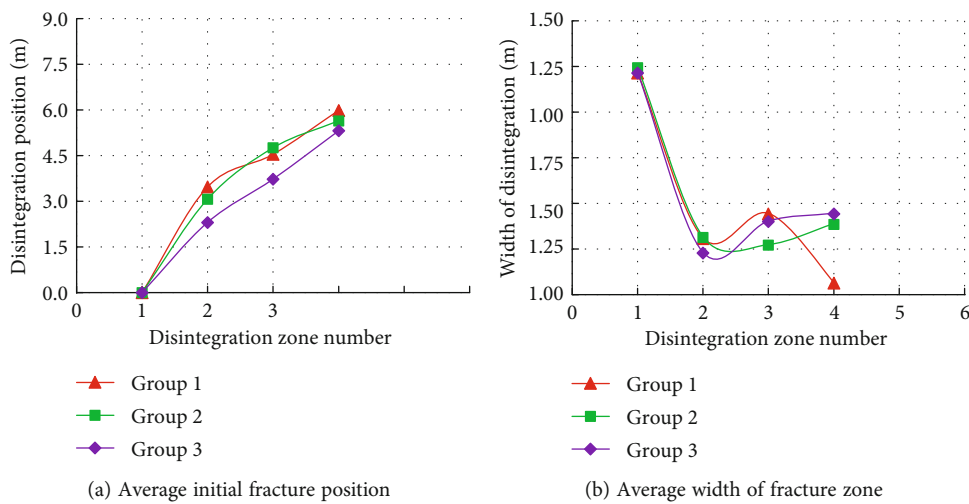
(b) Average width of fracture zone

FIGURE 19: Distribution diagram of zonal fracture under confining pressure in 213 floor roadway of Qujiang Coal Mine.

[27]. The peering results of typical drill holes are shown in Figure 17. The fracture zones above 0.2 m of different drill holes on each investigated section in the 213 floor roadway of Qujiang Coal Mine were delineated, and their distribution is shown in Figure 18. The fracture zone on the roadway surface was traditional excavation damaged zone. Multiple fracture zones appear from the roadway surface to the interior of surrounding rock [28]. There existed generally 4–5 fracture zones in the surrounding rock on each roadway section, and the fractures were gradually reduced from the roadway center toward the two sides, which was consistent with the previous theoretical study results.

The average initial positions (distance from the roadway wall) of the fracture zones in the surrounding rock at different positions within 15 m range from the upper and lower walls of the surrounding rock above the test roadway, as well as the average width of the fracture zone, were further calculated. The fracture laws and distribution in the surrounding rock of 213 floor roadway in Qujiang Coal Mine are shown in Figure 19. The fracture zone basically presented a linear increase trend with the increase in the distance from the tunneling head-on (i.e., the fracture zone was enlarged with

the pressure relief time), which coincided with the theory of rheological effect in the pressure relief of the roadway.

4.2.3. Initial Gas Flow in Drill Holes. The investigation results of gas flow in the drill holes arranged in the overlying coal seam of 213 floor roadway in Qujiang Coal Mine and the maximum increase amplitudes are shown in Figures 20 and 21, respectively.

The gas flow in the drill hole rightly above the floor roadway was the maximum, followed by those at 7.5 m and 15 m from the two sides of the roadway. The gas flow in the drill holes at the same position presented a gradual attenuation trend with the time. Therefore, the pressure relief effect of the coal seam above the floor roadway was gradually weakened from the center line to the two sides but strengthened as the pressure relief time was lengthened, which was identical with the previous study results. The initial gas flow per meter in the drill hole rightly above the pressure–relief floor roadway and those at 7.5 m and 15 m from the two sides were increased to 14.39, 9.90, and 4.41 times that in the original coal seam, respectively, fully manifesting that the pressure relief effect of floor roadway was significant.
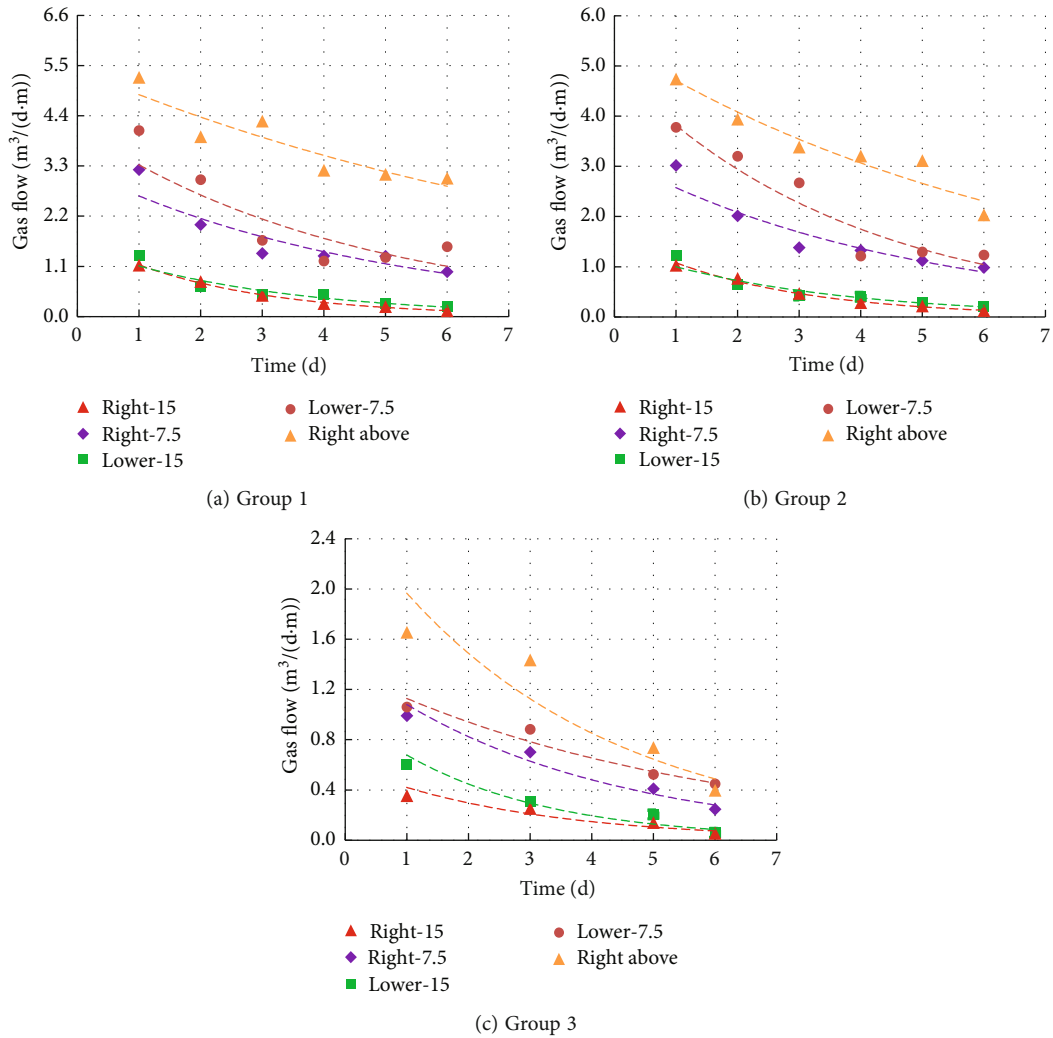
(a) Group 1

(b) Group 2

(c) Group 3

Figure 20: Variation diagram of gas flow in drill holes in 213 floor roadway of Qujiang Coal Mine.
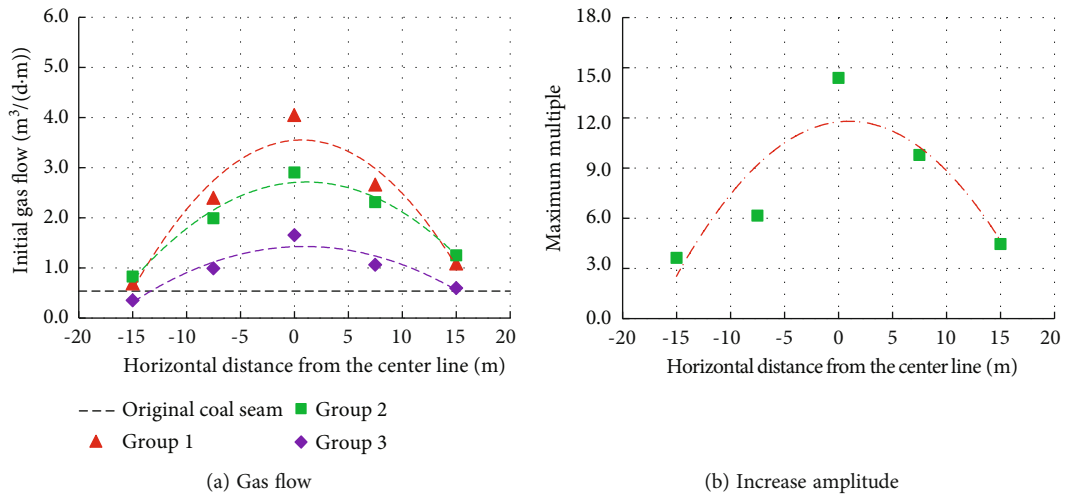

(a) Gas flow

(b) Increase amplitude

Figure 21: Change curve chart of initial gas flow in drill holes in 213 floor roadway of Qujiang Coal Mine.

5. Main Conclusions

(1) The unloading test of gas-bearing coal shows that the axial strain declines slowly after the rapid reduction initially during the unloading process of axial stress. The higher the confining pressure is, the greater the axial stress and strain in case of specimen failure will be. Moreover, the specimen can more easily reach the failure point due to the axial pressure relief under a high confining pressure, and the disturbance-induced deformation and failure degree of surrounding rock is higher in a deep high-stress roadway

(2) According to the similar simulation test results, the subsidence displacement on the roadway surface experiences three phases—slow, rapid, and stable deformations—with the increase in the load, and the fractures are continuously generated and propagating at the roadway roof. The displacement is the maximum at the roadway center line. The more distant from the roadway center line is, the smaller the displacement will be, and the displacements will show the symmetric distribution laws. The scope of influence of floor roadway excavation on the pressure relief of overlying rock strata reaches over 10 m. The tensile strain is generated within 15.6 m range at the two sides of the coal seam at 11.25 m away from the roadway roof, and the pressure relief state is manifested within this range

(3) The investigation results of displacement and failure in the overlying strata of deep floor roadway imply that the displacements of surrounding rock at different positions above the floor roadway are featured by the alternate crest and trough variation. Zonal fracture takes place inside the surrounding rock, and the deformation of surrounding rock and fracture zones are the maximum at the roadway center line and gradually reduced at the two sides. Moreover, the pressure relief effect is better if the distance from the tunneling face is greater and the pressure relief time is longer. The initial gas emission in the drill holes rightly above the roadway and those at 7.5 m and 15 m from the two sides reach 14.39, 9.90, and 4.41 times that in the original coal seam, hinting a highly apparent roadway pressure relief effect

(4) The stress level in the overlying coal and rock strata can be reduced in advance by arranging a short-distance floor roadway beneath the coal roadway to be mined to prevent and control the high-stress induced hazards in the deep mine. Hence, the pressure relief method through the short-distance floor roadway proposed in this study is feasible, thereby providing reference for the hazard prevention and control in other mines with similar conditions

Data Availability

The known data in this paper come from practical engineering case data, which are reliable and available.

Conflicts of Interest

The authors declare that they have no conflicts of interest.

Acknowledgments

References

[1] G. Cui, "Permeability improved technology of low permeability seams group in underground mine," *Coal Science and Technology*, vol. 44, no. 5, pp. 151–154, 2016.

[2] Y. Liu, Z. Zhang, B. Deng, and M. Li, "Liquid carbon dioxide fracturing application and its effect on gas drainage in low permeability coal seams of underground coal mine," *Energy Sources Part A Recovery Utilization and Environmental Effects*, vol. 106, pp. 1–13, 2019.

[3] C. J. Lian, C. M. Guo, Z. Y. Deng, and H. Y. Ma, "Spatial gas control technology and application of first mining protective layer of coal seam group with high gas outburst," *Coal Mining*, vol. 24, no. 1, pp. 124–127, 2019.

[4] X. Cheng, G. M. Zhao, Y. M. Li, X. R. Meng, C. L. Dong, and W. S. Xu, "Study on relief-pressure antireflective effect and gas extraction technology for mining soft rock protective seam," *Journal of Mining & Safety Engineering*, vol. 35, no. 5, pp. 1045–1053, 2018.

[5] M. J. Zhang, J. J. Shu, and J. T. Hua, "Anti-burst technology of gas strip in pre-extracted coal roadway with single coal seam floorway," *Coal Mine Safety*, vol. 42, no. 6, pp. 30–32, 2011.

[6] Z. Wang, *New Classification and Induced Transformation Conditions of Coal-Rock Gas Dynamic Disasters*, Chongqing University, 2010.

[7] L. Yuan, "Control of coal and gas outbursts in Huainan mines in China: a review," *Journal of Rock Mechanics and Geotechnical Engineering*, vol. 8, no. 4, pp. 559–567, 2016.

[8] D. J. Lei, C. W. Li, Z. M. Zhang, and Y. Zhang, "Coal and gas outburst mechanism of the "Three Soft" coal seam in western Henan," *Mining Science and Technology (China)*, vol. 20, no. 5, pp. 712–717, 2010.

[9] X. H. Sun and T. Li, *Theory and Technology for Preventing and Controlling Gas Dynamical Disasters of Compound Briquette and Rock in Deep Mines*, Science Press, Beijing, 2011.

[10] Z. J. Ren, "Application of hydraulic punching technology in seam gas drainage in Yuwu coal mine," *Coal Engineering*, vol. 51, no. 3, pp. 65–70, 2019.

[11] M. J. Liu, K. Cui, Y. W. Liu, Q. G. Deng, and Z. Liu, "Analysis on outburst prevention mechanism of borehole hydraulic flushing measures for deep and low permeability seam," *Coal Science and Technology*, vol. 40, no. 2, pp. 45–48, 2012.

[12] Q. B. Mou, Z. M. Yan, and J. Zhang, "High efficiency gas drainage technology of hydraulic fracturing with directional long drilling in underground coal mine," *Coal Science and Technology*, vol. 48, no. 7, pp. 296–303, 2020.

[13] S. G. Li, W. Z. Jiang, B. S. Jia, and R. S. Nie, "Application and prospect of fracturing and permeability enhancement

technology in low permeability coal seam," *Coal Science and Technology*, vol. 45, no. 6, pp. 35–42, 2017.

[14] J. J. Cao, "Application research on regional outburst prevention technology of ultra-high pressure hydraulic slot pressure in relief drainage area," *Coal Science and Technology*, vol. 48, no. 6, pp. 88–94, 2020.

[15] H. M. Yang, "Research status and development tendency of hydraulic cutting technology for pressure relief and permeability increasing of deep coal seam," *Safety in Coal Mines*, vol. 49, no. 6, pp. 147–151, 2018.

[16] Y. L. Li, Y. Liu, S. Wang, and Q. X. Wang, "Research and application of deep hole pre-splitting blasting technology for permeability enhancement in high gas and low permeability coal seam," *Journal of Safety Science and Technology*, vol. 16, no. 9, pp. 71–76, 2020.

[17] M. J. Gong, P. Chi, and M. J. Zhang, "Permeability increase with deep borehole controlled pre-cracking blasting technology in low permeability and high gassy seam," *Coal Science and Technology*, vol. 40, no. 10, pp. 69–72, 2012.

[18] W. L. Pu and Y. W. Bi, "Permeability improvement gas drainage technology with deep borehole accumulated energy hydraulic blasting of low permeability seam," *Coal Science and Technology*, vol. 42, no. 5, pp. 37–40, 2014.

[19] D. Y. Shang, L. Peng-fei, X. Y. YU, and H. J. Zhang, "Permeability improved technology and practices with deep borehole energy accumulation blasting in low permeability seam," *Coal Science and Technology*, vol. 40, no. 12, pp. 48–51, 2012.

[20] N. Jia, "Joint application research on screen pipe protection hole and CO^2 phase change fracturing technology in low permeability and soft coal seam," *Safety in Coal Mines*, vol. 49, no. 1, pp. 153–156, 2018.

[21] H. P. Xie, F. Gao, and Y. Ju, "Research and development of rock mechanics in deep ground engineering," *Chinese Journal of Rock Mechanics and Engineering*, vol. 34, no. 11, pp. 2161–2178, 2015.

[22] H. P. Xie, "Research review of the state key research development program of China: deep rock mechanics and mining theory," *Journal of China Coal Society*, vol. 44, no. 5, pp. 1283–1305, 2019.

[23] W. X. Li, G. Wang, W. Z. Du et al., "Development and application of a true triaxial gas-solid coupling testing system for coal seepage," *Rock and Soil Mechanics*, vol. 37, no. 7, pp. 2109–2118, 2016.

[24] G. Wang, Z. Y. Liu, P. F. Wang, W. R. Wang, C. Fan, and X. Song, "Experimental study on shear seepage characteristics of true triaxial coal body under the consideration of gas adsorption," *Journal of Mining and Safety Engineering*, vol. 36, no. 5, pp. 1061–1070, 2019.

[25] T. F. Xie, *Study of Mechanism and Control Technology of Floor Heave under High Stress in Deep Roadway*, AnHui University of Science and Technology, 2018.

[26] M. Yang, X. Z. Hua, Z. G. Liu, and Q. J. Liu, "A multifunctional test apparatus for deep mining engineering," *Safety in Coal Mines*, vol. 50, no. 5, pp. 126–129, 2019.

[27] Z. H. Wang, "Displacement failure of deep surrounding rock and optimization of sealing process of through holes," *China Coal*, vol. 41, no. 12, pp. 105–109, 2015.

[28] S. C. Li, H. P. Wang, Q. H. Qian et al., "In-situ monitoring research on zonal disintegration of surrounding rock mass in deep mine roadways," *Chinese Journal of Rock Mechanics and Engineering*, vol. 27, no. 8, pp. 1545–1553, 2008.